Digital Object Identifier: 10.1109/ULTSYM.2008.0314

Two Approaches for Tomographic Density Imaging Using Inverse Scattering

Roberto J. Lavarello and Michael L. Oelze
Bioacoustics Research Laboratory
Department of Electrical and Computer Engineering
University of Illinois at Urbana-Champaign
Urbana, IL 61801
Email: lavarell@illinois.edu

***Abstract*— Most acoustic tomography methods neglect density variations in order to obtain speed of sound and attenuation profiles. However, density may provide additional sources of image contrast. In this work, two approaches for density imaging using inverse scattering were explored through simulations in order to evaluate the feasibility of density imaging. The first method consisted of inverting the wave equation by solving for a single functional that depended on both speed of sound and density variations. Density profiles were separated by combining reconstructions at two frequencies (DF-DBIM approach). The second method consisted of solving for two functionals simultaneously: one that depended only on compressibility and one that depended only on density variations. A T-matrix approach was used to relate these functionals to the scattered data. The DF-DBIM approach allowed separation of density and speed of sound profiles at low termination tolerance values and less than an order of magnitude between the largest and smallest frequencies used. However, the convergence of DF-DBIM was compromised even when moderate (around 2%) termination tolerances were used. The T-matrix approach converged when multiple frequency data was used, but required a ka product smaller than one at the lowest frequency. The DF-DBIM requires a very high SNR to obtain reliable quantitative density reconstructions, while the T-matrix approach requires excessively large bandwidths when imaging large targets. These limitations will serve as reference points for further algorithmic improvements required for practical implementation of density imaging on ultrasound tomographic systems.**

I. MOTIVATION

Ultrasonic computerized tomography (UCT) is an imaging modality used to reconstruct quantitative images of acoustic properties. Several approaches, including ray propagation algorithms [1], diffraction tomography [2], and inverse scattering methods [3] have been developed to reconstruct quantitative images of speed of sound and acoustic attenuation.

However, experimental evidence is available in the literature suggesting that relative density changes in tissues may be comparable in magnitude to relative sound speed changes [4]. The effects of variable density in the reconstruction of sound speed were observed to result in overshoots of sound speed estimates at the edges of objects where density underwent abrupt changes [5]. Even further, density may also provide additional sources of image contrast.

The number of UCT studies that consider variable density is limited. Variable density UCT was introduced in the context of single scattering formulations [6], [7]. However, the fact that these works are based on linearized scattering theory limits their applicability. Two classes of variable density inverse scattering algorithms have been identified, which consist of inverting the wave equation by 1) solving for a single functional that depended on both speed of sound and density variations, and using multiple frequency data to isolate density information [8], [9], and 2) solving for two functionals simultaneously: one that depended only on compressibility and one that depended only on density variations [10], [11]. In the present work the performance of the two classes of variable density inverse scattering algorithms, as quantified by the reconstruction root mean square error (RMSE), was analyzed through simulations. For all cases, analytic solutions were used to generate the synthetic scattered data.

II. THE DUAL FREQUENCY DBIM APPROACH (DF-DBIM)

The integral wave equation for a harmonic field at frequency ω can be written as [12]

$$p(\vec{r}) = e_s(\vec{r}) + \int_\Omega d\vec{r}\,'\mathcal{O}(\vec{r}\,')p(\vec{r}\,')G_0(\vec{r},\vec{r}\,'), \qquad (1)$$

where $e_s(\vec{r})$ is the incident field caused by a source located at $\vec{r}_s$, $s = 0, 1, ..., N_s$ and $G_0(\vec{r},\vec{r}\,')$ is the free space Green's function. The object function $\mathcal{O}(\vec{r})$ is given by

$$\mathcal{O}(\vec{r}) = \left(\left(\frac{\omega}{c(\vec{r})}\right)^2 - \left(\frac{\omega}{c_0}\right)^2\right) - \rho^{1/2}(\vec{r})\nabla^2\rho^{-1/2}(\vec{r}). \qquad (2)$$

where $\rho(\vec{r})$ and $c(\vec{r})$ are the density and sound speed profiles. Equation (1) can be discretized using the method of moments (MoM) and written in matrix form, both for the pressure field inside the computational domain $\bar{p}$ and the scattered field outside the computational domain $\bar{p}^{sc}$, as

$$\bar{p} = \left(\bar{I} - \bar{C}\cdot\mathcal{D}(\bar{\mathcal{O}})\right)^{-1}\cdot\bar{p}^{inc} \qquad (3)$$
$$\bar{p}^{sc} = \bar{D}\cdot\mathcal{D}(\bar{\mathcal{O}})\cdot\bar{p}, \qquad (4)$$

where $\bar{D}$ is a matrix with the Green's coefficients from each pixel to the receivers, $\bar{C}$ is a matrix with the Green's coefficients among all the pixels, and $\mathcal{D}$ is an operator that transforms a vector into a diagonal matrix.

The distorted Born iterative method [3] consists of inverting the wave equation using a Newton-type iteration. A trial $\bar{\mathcal{O}}_{(0)}$ is chosen for which the corresponding scattered field is calculated. Next, the object function is updated as $\bar{\mathcal{O}}_{(n+1)} = \bar{\mathcal{O}}_{(n)} + \Delta\bar{\mathcal{O}}_{(n)}$. The update $\Delta\bar{\mathcal{O}}_{(n)}$ is given by

$$\Delta\mathcal{O}_{(n)} = \underset{\Delta\mathcal{O}}{\arg\min} \, ||\Delta\bar{p}^{sc} - \bar{F}_{(n)} \cdot \Delta\mathcal{O}||_2^2 + \gamma||\Delta\mathcal{O}||_2^2, \quad (5)$$

where $\Delta\bar{p}^{sc}$ contains the difference between the predicted and measured scattered fields and γ is the regularization parameter. The Frechet derivative matrix $\bar{F}_{(n)}$ is composed of N_s stacked matrices $\bar{F}_s$ of the form

$$\bar{F}_s = \bar{D} \cdot \left\{\bar{I} - \mathcal{D}(\bar{\mathcal{O}}) \cdot \bar{C}\right\}^{-1} \cdot \mathcal{D}(\bar{p}_s), \quad (6)$$

The iterative process is repeated until the residual error (RRE), given by RRE $= ||\Delta\bar{p}^{sc}||_2/||\bar{p}^{sc}||_2$, falls within a desired termination tolerance. A linear combination of the reconstructions $\mathcal{O}_i$ at frequencies ω_i, $i = 1, 2, ..., N_f$ allows the separation of $c(\vec{r})$ and $\rho(\vec{r})$ contributions. Specifically,

$$\mathcal{F}_\rho(\vec{r}) = \frac{\left(\sum_{i=1}^{N_f}\omega_i^2\right)\left(\sum_{i=1}^{N_f}\omega_i^2\mathcal{O}_i(\vec{r})\right) - \left(\sum_{i=1}^{N_f}\omega_i^4\right)\left(\sum_{i=1}^{N_f}\mathcal{O}_i(\vec{r})\right)}{N_f\sum_{i=1}^{N_f}\omega_i^4 - \left(\sum_{i=1}^{N_f}\omega_i^2\right)^2}, \quad (7)$$

where $\mathcal{F}_\rho = \rho^{1/2}(\vec{r})\nabla^2\rho^{-1/2}(\vec{r})$. The simplest approach, the dual frequency DBIM (DF-DBIM) [8], [9], is to use $N_f = 2$ because for a fixed spatial resolution (dictated by the maximum frequency f_0 used) only one parameter (the lowest frequency f_{min} used) has to be chosen. To obtain ρ profiles using DF-DBIM, the differential equation

$$\begin{aligned} \nabla^2 u(\vec{r}) - \mathcal{F}_\rho(\vec{r})u(\vec{r}) &= \mathcal{F}_\rho(\vec{r}), \vec{r} \in \Omega \\ u(\vec{r}) &= 0, \vec{r} \notin \Omega \end{aligned} \quad (8)$$

has to be solved, where $u(\vec{r}) = \left(\rho_r^{-1/2}(\vec{r}) - 1\right)$. Equation (8) was solved by converting it to a matrix equation, with ∇^2 implemented using a finite difference template.

The effect of some parameters in the quality of ρ reconstructions are shown in Fig. 1. The minimum frequency f_{min} was varied between $0.9f_0$ and $0.1f_0$ and the DBIM termination tolerance was set to 0.1%. Cylinders with radii of λ_0, $2\lambda_0$ and $4\lambda_0$ were reconstructed, where $\lambda_0 = c_0/f_0$. Both the dependence on the value of the relative density ρ_r compared to the relative speed of sound c_r (fixed $\Delta\phi = 0.9\pi$ and ρ_r values of $1/c_r$, $1/c_r^2$, and $1/c_r^4$, where $\Delta\phi = 2k_0a(c_r^{-1} - 1)$ is the maximum excess phase accumulated by the acoustic wave when passing through the cylinder) and $\Delta\phi$ (fixed $\rho_r = 1/c_r$ and $\Delta\phi$ values of -0.9π, 0.45π, and -0.45π) were studied. Larger density changes required the use of lower f_{min} values for optimum accuracy at the cost of reduced spatial resolution. In general, larger cylinder radii resulted in more unstable reconstructions when f_0 and f_{min} were relatively close. Therefore, the optimum f_{min} value depends on the actual imaging target, but results suggest that reliable results can only be obtained when f_{min} is small compared to f_0.

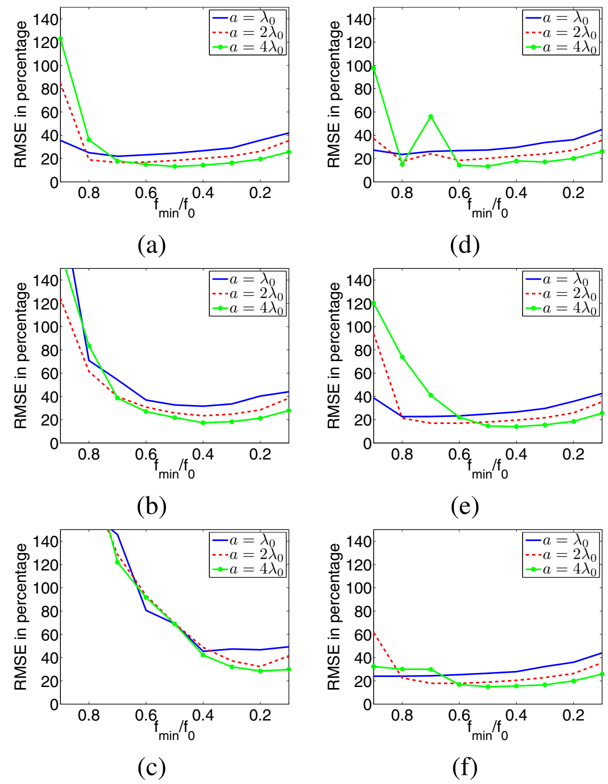

Fig. 1. RMSEs in density reconstructions using the DF-DBIM approach. The corresponding properties of the cylinders are (a) $\rho_r = 1/c_r$, $\Delta\phi = 0.9\pi$, (b) $\rho_r = 1/c_r^2$, $\Delta\phi = 0.9\pi$, (c) $\rho_r = 1/c_r^4$, $\Delta\phi = 0.9\pi$, (d) $\rho_r = 1/c_r$, $\Delta\phi = -0.9\pi$, (e) $\rho_r = 1/c_r$, $\Delta\phi = 0.45\pi$, and (f) $\rho_r = 1/c_r$, $\Delta\phi = -0.45\pi$. The DBIM termination tolerance was set to 0.1%.

The effect of the DBIM termination tolerance was also studied. Figure 2 shows the RMSE curves when reconstructing an $a = 2\lambda_0$, $\rho_r = 1/c_r$, $\Delta\phi = 0.9\pi$ cylinder using tolerances of 0.1%, 1%, and 2%. The RMSE curves behaved smoothly when the DBIM tolerance was low (0.1%), but degraded significantly as the tolerance increased unless $f_{min} \ll f_0$. This effect has a direct impact on practical implementations, where the termination tolerance has to be larger than the noise floor in order to avoid divergence.

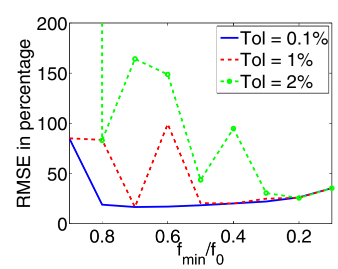

Fig. 2. Effect of the DBIM termination tolerance when reconstructing a cylinder with radius $2\lambda_0$, $\rho_r = 1/c_r$ and $\Delta\phi = 0.9\pi$ using termination tolerances of 0.1%, 1%, and 2%.

III. THE T-MATRIX APPROACH

The total acoustic field produced at some point $\vec{r}_p$ in space can be expressed as [10]

$$p(\vec{r}_p) = \psi^t(\vec{r}_p - \vec{r}_s) \cdot \bar{f}_s + \sum_{m=1}^{N} \psi^t(\vec{r}_p - \vec{r}_m) \cdot \bar{a}_m \tag{9}$$

where $\vec{r}_s$ is the location of the source, $\vec{r}_m$ is the location of the m-th subscatterer, $\psi(\vec{r})$ is a vector of cylindrical harmonics, and $\bar{f}_s$ and $\bar{a}_m$ are vectors containing the amplitudes of the cylindrical harmonic fields generated by the source and the m-th subscatterer, respectively. Equation (9) can be rewritten using the j-th subscatterer as the origin for all the cylindrical harmonics using the addition theorem of Bessel functions as

$$p(\vec{r}_p) = \psi^t(\vec{r}_{pj}) \cdot \bar{a}_j + \hat{\psi}^t(\vec{r}_{pj}) \cdot \left(\sum_{m \neq j} \bar{\alpha_{jm}} \cdot \bar{a}_m + \bar{e}_{js} \right)$$

$$[\alpha_{jm}]_{kl} = H^{(1)}_{k-l}(k_0|\vec{r}_{mj}|) e^{-i(k-l)\theta_{mj}}, \tag{10}$$

where $\left[\hat{\psi}(\vec{r})\right]_k = J_k(k_0 r) e^{il\theta}$ and, for line sources, $[\bar{e}_{js}]_k = H^{(1)}_k(k_0|\vec{r}_{sj}|) e^{-ik\theta_{sj}}$. If $h \ll \lambda$, the harmonics $l = 0, 1, -1$ are sufficient to characterize the scattering process. The vector of equivalent induced sources $\bar{a}_s$ when the transmitter is at the position $\vec{r}_s$ is approximated as

$$\left\{ \bar{I} - \mathcal{D}\left(\bar{R}\right) \cdot \bar{A} \right\} \cdot \bar{a}_s = \mathcal{D}\left(\bar{R}\right) \cdot \bar{e}_s \tag{11}$$

where $\bar{A}$ is a matrix containing the $[\alpha_{jm}]_{kl}$ coefficients, $\bar{R}$ are the scattering coefficients at the surface of the pixels for the harmonics $k = 0, 1, -1$, and $\bar{e}_s$ is a vector whose elements are given by $\bar{e}_{js}$. If the total pressure $\bar{e}_{ts}$ at the scatterer is defined such that $\bar{a}_s = \mathcal{D}(\bar{R}) \cdot \bar{e}_{ts}$, then from Eq. (11),

$$\bar{e}_{ts} = \left[\bar{I} - \bar{A} \cdot \mathcal{D}(\bar{R})\right]^{-1} \cdot \bar{e}_s. \tag{12}$$

The T-matrix formulation can be inverted using the same iterative process used in the DBIM. The object function vector is here defined as $\mathcal{O} = \left[\{\bar{R}\}_{k=0}; \{\bar{R}\}_{k=1}\right]$ because $R_1(\kappa, \rho) = R_{-1}(\kappa, \rho)$. Even further, if $h \ll \lambda$ then $\{\bar{R}\}_{k=0}$ and $\{\bar{R}\}_{k=1}$ depend only on compressibility and density, respectively. By analogy with Eq. (6), the Frechet derivative matrix blocks $\bar{F}_s$ are given by

$$\bar{F}_s = \bar{\psi} \cdot \left\{\bar{I} - \mathcal{D}(\bar{R}) \cdot \bar{A}\right\}^{-1} \cdot \mathcal{M}(\bar{e}_{ts}) \tag{13}$$

$$\mathcal{M}(\bar{e}_{ts}) = \begin{bmatrix} \mathcal{D}(\{\bar{e}_{ts}\}_{k=0}) & 0 \\ 0 & \mathcal{D}(\{\bar{e}_{ts}\}_{k=1}) \\ 0 & \mathcal{D}(\{\bar{e}_{ts}\}_{k=-1}) \end{bmatrix} \tag{14}$$

The performance of the T-matrix approach was studied using the same simulation sets than in Section II, with a termination tolerance of 2%. Data at N_f logarithmically spaced frequencies between $f_{min} = 2^{-N_f+1} f_0$ and f_0 were sequentially processed. The results are presented in Fig. 3. For all cases, the scatterer size was the main factor that affected the reconstruction quality. A minimum frequency f_{min} such that $ka \approx 1$ was required in order to obtain convergence for the density reconstructions.

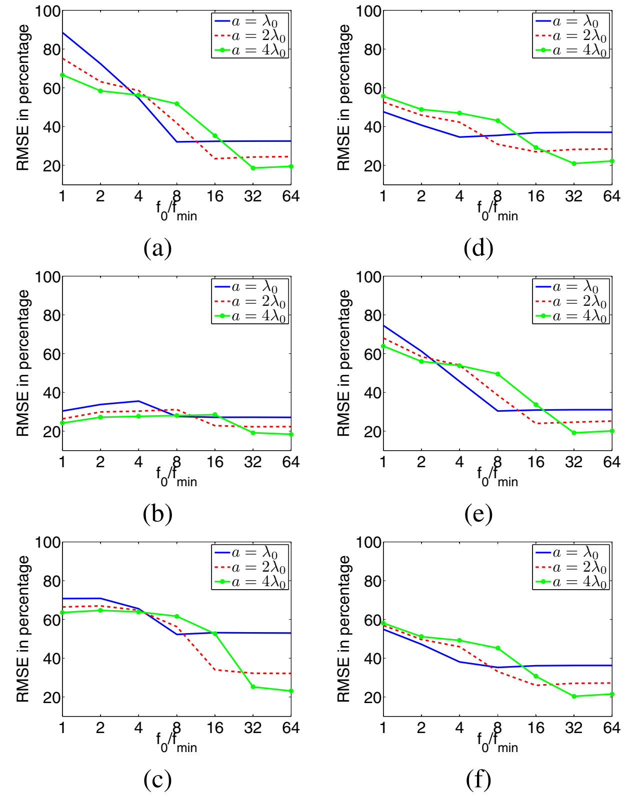

Fig. 3. RMSEs in density reconstructions using frequency hopping and the T-matrix approach. The corresponding properties of the cylinders are (a) $\rho_r = 1/c_r$, $\Delta\phi = 0.9\pi$, (b) $\rho_r = 1/c_r^2$, $\Delta\phi = 0.9\pi$, (c) $\rho_r = 1/c_r^4$, $\Delta\phi = 0.9\pi$, (d) $\rho_r = 1/c_r$, $\Delta\phi = -0.9\pi$, (e) $\rho_r = 1/c_r$, $\Delta\phi = 0.45\pi$, and (f) $\rho_r = 1/c_r$, $\Delta\phi = -0.45\pi$. The T-matrix termination tolerance was set to 2% for all simulations.

IV. FURTHER DEVELOPMENTS

Even though both the DF-DBIM and T-matrix approaches suffer from limitations that prevent their practical use in experimental systems, the results presented here can serve as reference points for further algorithmic developments. An alternative data processing scheme, termed here the multiple frequency DBIM approach (MF-DBIM), uses (7) with several frequencies between f_{min} and f_0. A comparison of the DF-DBIM and MF-DBIM performance when reconstructing a circular cylinder with $\Delta\phi = 0.9\pi$, $\rho_r = 1/c_r$, and $a = 2\lambda$ is shown in Fig. 4. The results suggest that the proper use of multiple frequency information allows for a better extraction of density information.

An example is shown in Fig. 5 for the reconstruction of a computer phantom using all methods studied in this work. The scattered field was calculated analytically using boundary conditions and the addition theorem. Single frequency reconstructions were obtained with a termination tolerance of 5% in all cases. The DF-DBIM, T-matrix, and MF-DBIM reconstructions were obtained using f_{min} values of $f_0/2$, $f_0/64$, and

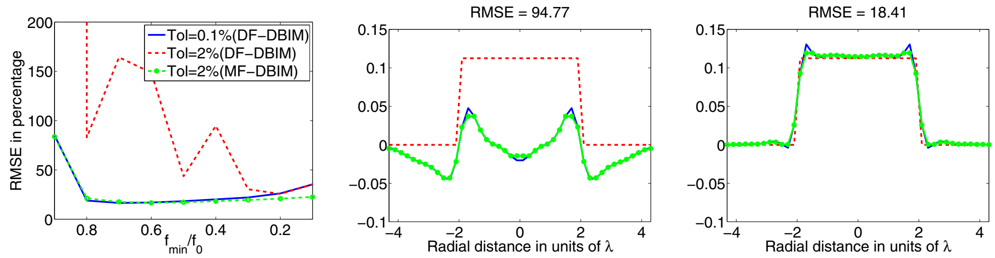

(a) (b) (c)

Fig. 4. The use of MF-DBIM for density imaging. (a) RMSE curves obtained with DF-DBIM and MF-DBIM. (b) Reconstructed profile using DF-DBIM and $f_{min} = 0.4f_0$. (c) Reconstructed profile using MF-DBIM and $f_{min} = 0.4f_0$. For (b) and (c), the ideal (red), reconstructed (blue) and median filtered(green) profiles are shown, and 2% termination tolerance was used.

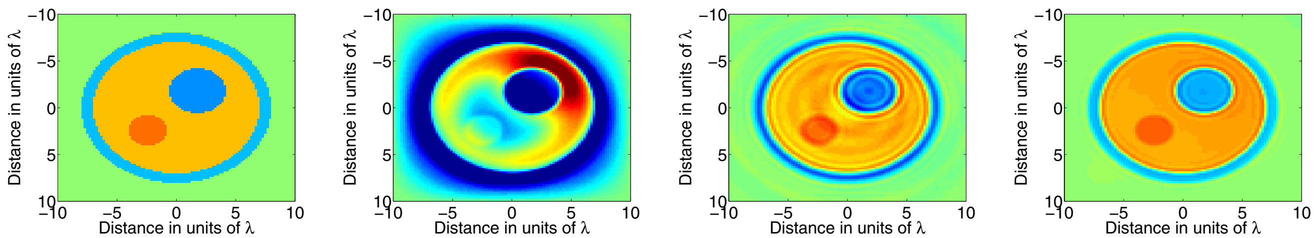

(a) (b) (c) (d)

Fig. 5. Density reconstructions of a computer phantom using three different algorithms. (a) Ideal density profile. (b) DF-DBIM reconstruction with $f_{min} = f_0/2$. (c) T-matrix reconstruction with $f_{min} = f_0/64$. (d) MF-DBIM reconstruction with $f_{min} = f_0/2$. The relative density range is limited in all images between 0.95 and 1.05.

$f_0/2$, respectively. The RMSEs in the reconstructions were 212.20%, 31.48%, and 24.54% when using the DF-DBIM, T-matrix, and MF-DBIM approaches, respectively. Therefore, the MF-DBIM is able to improve upon the convergence characteristics of DF-DBIM while using a significantly smaller bandwidth than the T-matrix approach.

V. Conclusions

The present work presents a joint performance analysis of two inverse scattering algorithms (DF-DBIM and T-matrix) designed to reconstruct density profiles. The performance of both approaches was studied under different conditions considering the effects of the cylinder size relative to the acoustic wavelength, density contrast, and speed of sound contrast.

The findings of this study indicated that the DF-DBIM requires a very high SNR in order to converge to a proper solution. The T-matrix approach, on the other hand, requires a very large bandwidth which scales with the size of the imaging target. Therefore, neither algorithm appears amenable for direct experimental implementation.

However, algorithmical variations of these approaches may result in improved performance. This was exemplified through the MF-DBIM approach, which was observed to outperform both the DF-DBIM and T-matrix approaches when reconstructing a computer phantom.

VI. Acknowledgements

The authors would like to thank Dr. Stephen Bond for discussions on the DF-DBIM algorithm. This work was supported in part by a grant from the 3M corporation.

References

[1] J. Greenleaf, S. Johnson, W. Samayoa, and F. Duck, "Algebraic reconstruction of spatial distributions of acoustic velocities in tissue from their time-of-flight profiles," in *Acoustical Holography*, vol. 6, 1975, pp. 71–90.

[2] B. Robinson and J. Greenleaf, "The scattering of ultrasound by cylinders: Implications for diffraction tomography," *Journal of the Acoustical Society of America*, vol. 80, no. 1, pp. 40–49, July 1986.

[3] W.C. Chew and Y.M. Wang, "Reconstruction of two-dimensional permittivity distribution using the distorted Born iterative method," *IEEE Transactions on Medical Imaging*, vol. 9, no. 2, pp. 218–225, June 1990.

[4] S.A. Goss, R.L. Johnston, and F. Dunn, "Comprehensive compilation of empirical ultrasonic properties of mammalian tissues," *Journal of the Acoustical Society of America*, vol. 64, no. 2, pp. 423–457, August 1978.

[5] R.J. Lavarello and M.L. Oelze, "A study on the reconstruction of moderate contrast targets using the distorted Born iterative method," *IEEE Transactions on Ultrasonics, Ferroelectrics, and Frequency Control*, vol. 55, no. 1, pp. 112–124, January 2008.

[6] S.J. Norton, "Generation of separate density and compressibility images in tissue," *Ultrasonic Imaging*, vol. 5, no. 3, pp. 240–252, July 1983.

[7] A.J. Devaney, "Variable density acoustic tomography," *Journal of the Acoustical Society of America*, vol. 78, no. 1, pp. 120–130, July 1985.

[8] M.J. Berggren, S.A. Johnson, B.L. Carruth, W.W. Kim, F. Stenger, and P.K. Kuhn, "Ultrasound inverse scattering solutions from transmission and/or reflection data," in *Proceedings of the SPIE*, vol. 671, 1986, pp. 114–121.

[9] S. Kwon and M. Jeong, "Ultrasound inverse scattering determination of speed of sound, density and absorption," in *IEEE Ultrasonics Symposium*, 1998, pp. 1631–1634.

[10] J. Lin and W. Chew, "Ultrasonic imaging by local shape function method with CGFFT," *IEEE Transactions on Ultrasonics, Ferroelectrics, and Frequency Control*, vol. 43, no. 5, pp. 956–969, September 1996.

[11] K.W.A. van Dongen and W.M.D. Wright , "A full vectorial contrast source inversion scheme for three-dimensional acoustic imaging of both compressibility and density profiles," *Journal of the Acoustical Society of America*, vol. 121, no. 3, pp. 1538–1549, March 2007.

[12] S.A. Johnson, F. Stenger, C. Wilcox, J. Ball, and M.J. Berggren, "Wave equations and inverse solutions for soft tissue," in *Acoustical Imaging*, vol. 11, 1982, pp. 409–424.